How to cite: *Angew. Chem. Int. Ed.* **2025**, *64*, e202418447
doi.org/10.1002/anie.202418447

VIP Electrochemical Modelling Very Important Paper

Deep Neural Network Enhanced Mesoscopic Thermodynamic Model for Unlocking the Electrode/Electrolyte Interface

*Haolan Tao[+], Sijie Wang[+], Honglai Liu, and Cheng Lian**

Abstract: Structure and properties of the electrode/electrolyte interface significantly influence the electrochemical processes of energy storage and conversion, yet the challenge lies in accurate description of both molecular characteristics and external field effects. Here, we develop a mesoscopic thermodynamic model that calculates the thermodynamic properties of electrolytes based on chemical potential, and its efficiency is enhanced by a deep neural network. The deep neural network enhanced mesoscopic thermodynamic (DeepMT) model effectively bridges the gap between micro-level characteristics of ions and macro-level effects of external field, enabling precise presentation of ion density distributions over complex conditions. Our result indicates that the DeepMT model not only demonstrates a computational efficiency improvement of approximately four orders of magnitude over direct theoretical calculations, but also accurately predicts interface properties including ion adsorption, surface charge, and differential capacitance through the statistical analysis of density distributions.

1. Introduction

Charged interfaces are prevalent in both natural systems[1] and human industrial.[2] The distribution of electrolyte and solvent near charged interfaces is highly heterogeneous.[3] Counter ions tend to accumulate at the interface, while co-ions are repelled away.[4] This distinctive interface structure is known as the electric double layer (EDL),[5] was first discovered and proposed by Helmholtz in 1853,[6] and was later improved and perfected by Gouy,[7] Chapman,[8] Stern,[9] Graham[10] and others. Due to the significant inhomogeneity of electrolyte distribution, the EDL shows unique properties which are markedly different from those of a homogeneous electrolyte.[11] The investigation and regulation of structure and properties of the EDL have become hot points of multiple research fields, including batteries,[3a] supercapacitors,[12] electrocatalysis,[13] and electrochemical sensors.[14] At an electrode/electrolyte interface, the structure of EDL, particularly ion distribution, directly influences the characteristics and efficiency of electrochemical processes.[15] The rapid and accurate description of ion distribution is essential for advancing EDL research and enhancing the performance of related technological applications.[16] However, it remains a challenge in establishing an effective integration of complex ion interactions at a microscopic scale and multiple external effects including electric, thermal, and flow fields at a macroscopic scale.

Numerous methods for studying the structure and properties of EDL have been established and developed. The mean-field method,[17] represented by Poisson–Boltzmann (PB) theory, simplifies the many-body problem into a single-body problem, facilitating the calculation and understanding of the system's overall behavior. However, its accuracy is limited, making it difficult to handle complex and extreme systems. Molecular dynamics (MD) simulations reveal the detailed dynamic behavior of a system by tracking the motion of atoms and molecules. They can accurately capture interactions and dynamic processes at the atomic level,[18] but their computational complexity is high and they are limited in time and length scales.[19] Grand canonical Monte Carlo (MC) simulation[20] calculates the equilibrium properties of a system at fixed temperature and chemical potential through random sampling. It has the advantage of handling large-scale systems, but it is computationally inefficient and requires an enormous number of samples to ensure accuracy. Classical density functional theory (CDFT)[21] is a statistical mechanics method that relates the free energy of a system to the density of individual particles, accounting for inter-particle interactions by calculating the excess free energy, which strikes a balance between computational accuracy and efficiency. Compared to MD and MC simulations, CDFT can yield consistent results[22] with much lower computational cost. As a classical mesoscopic thermodynamic model suitable for inhomogeneous particle systems, CDFT has become a crucial tool for describing the structure of the EDL and the interface behavior.[23] At present, a significant bottleneck in the development of CDFT is the low applicability to complex electrochemical interfaces, and the small research community. Here, we propose a mesoscopic thermodynamic model based on the CDFT, which utilizes the system potential to balance the microscopic description of electrolyte properties and the macroscopic representation of external field effects (Figure 1B). In the mesoscopic thermodynamic model, a thermodynamic potential at local position **r** is defined:

[*] Dr. H. Tao,[+] S. Wang,[+] Prof. Dr. H. Liu, Prof. C. Lian
State Key Laboratory of Chemical Engineering, School of Chemistry and Molecular Engineering, East China University of Science and Technology, Shanghai 200237 (P. R. China)
E-mail: liancheng@ecust.edu.cn

[+] These authors contributed equally to this work.

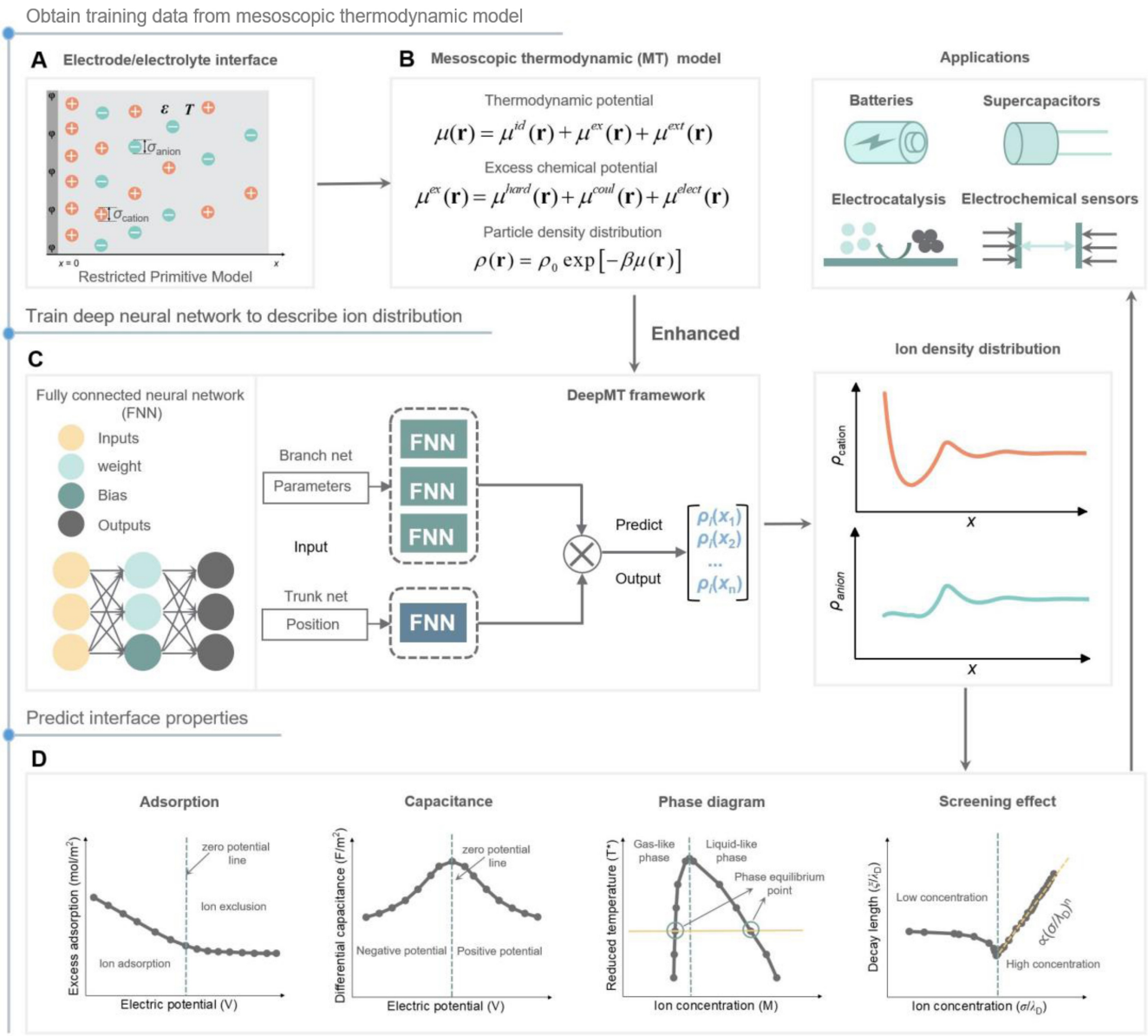

Figure 1. Flowchart of combining the mesoscopic thermodynamic model with the DeepONet framework. (A) For the targeted electrode/electrolyte interface, the electrolyte is in contact with an electrode at a potential of φ, where the anions and cations are modeled as hard spheres with a certain diameter and identical valence. (B) The thermodynamic potential μ is the core of the mesoscopic thermodynamic (MT) model, which is composed of ideal chemical potential, excess chemical potential and external potential. (C) The DeepONet, including three branch networks and one trunk network is used to construct the DeepMT framework. (D) Predicting interface properties such as adsorption capacity, capacitance (e.g. a bell shape differential capacitance-potential curve), phase diagram, and screening effect based on the results of ion density distribution. The ε, T, ξ, σ, and λ_D are the dielectric constant, temperature, decay length, ion diameter and Debye length, respectively.

$$\mu(\mathbf{r}) = \mu^{id}(\mathbf{r}) + \mu^{ex}(\mathbf{r}) + \mu^{ext}(\mathbf{r}),$$

where $\mu^{id}(\mathbf{r})$ represents the ideal chemical potential; $\mu^{ex}(\mathbf{r})$ represents the excess chemical potential, which is used to describe the multiple interactions between particles; and $\mu^{ext}(\mathbf{r})$represents the external potential, which is used to describe the effects of external field. The excess chemical potential $\mu^{ex}(\mathbf{r})$ can be expressed as the sum of several interactions:

$$\mu^{ex}(\mathbf{r}) = \mu^{hard}(\mathbf{r}) + \mu^{coul}(\mathbf{r}) + \mu^{elect}(\mathbf{r}),$$

where $\mu^{hard}(\mathbf{r})$, $\mu^{coul}(\mathbf{r})$, and $\mu^{elect}(\mathbf{r})$ represent the chemical potentials of hard-sphere interactions, Coulomb interactions, and electrostatic correlations, respectively. Once the thermodynamic potential of the system is obtained, the density distribution can be solved using the equation:

$$\rho(\mathbf{r}) = \rho_0 \exp[-\beta\mu(\mathbf{r})].$$

where $\rho(\mathbf{r})$ and ρ_0 are local and bulk ion number densities, respectively; and $\beta^{-1}=k_BT$ with k_B being the Boltzmann constant. The model provides a vivid presentation of the relationship between microscopic, mesoscopic and macroscopic thermodynamics, as the detailed discussion provided in Supporting Information (Figure S1). Since solving the mesoscopic thermodynamic model primarily relies on decomposing free energy into different excess terms, it requires solving numerous functionals related to free energy and density distribution. However, classical numerical methods, such as Picard iteration,[24] limit the solution efficiency of the mesoscopic thermodynamic model.

During recent years, the advancement of artificial intelligence technology has led to the widespread application of machine learning, particularly deep learning methods, in the fields of interface and fluid properties research.[25] The application of deep learning to physical models is underpinned by the universal approximation theorem, which posits that any function can theoretically be approximated by a neural network.[26] The advent of deep learning has catalyzed the revival and further advancement of the mesoscopic thermodynamic model.

Several studies have explored the integration of CDFT with deep learning methodologies.[27] The initial concept of integrating CDFT with machine learning methods was proposed by Lin et al.[27a] They conducted machine learning training based on datasets obtained from MC simulations. This approach allowed them to approximate the excess free energy functional (F^{ex}) of one-dimensional supercritical Lennard-Jones (LJ) fluids and provided accurate predictions of interfacial density distributions. Building on this work, Cat et al.[27b] employed similar combinatory methods to extend the simulation system from one-dimensional LJ fluids to three-dimensional LJ fluids. In contrast to the work of Lin[27a] and Cat,[27b] Sammüller[27c] directly established the relationship between the density distribution and the direct correlation function of the monomer through machine learning. The core idea behind these machine learning methods is to first approximate the functional, such as excess free energy and related functions, using machine learning techniques, and then derive the system′s density distribution. However, most studies are concentrated on specific systems and have not been generalized for universal comparison. Recently, Lu et al.[28] developed a novel neural network architecture, deep operator network (DeepONet), to rapidly solve various ordinary and partial differential equations through approximation. The authors have demonstrated the high accuracy and efficiency of this network architecture.

In this work, we introduce the DeepONet framework into the mesoscopic thermodynamic model to construct a deep neural network enhanced mesoscopic thermodynamic (DeepMT) model (Figure 1C). The used DeepONet framework contains three branch networks (branch1, branch2, and branch3) and a trunk network, each implemented as fully connected neural networks (FNN). The trunk network receives spatial coordinates x, while the electrode potential, bulk concentration, ion diameter, and dielectric constant are input into the three branch networks, respectively. The output is the ion density distribution $\rho(x)$ over various positions. Here, we use the DeepONet framework to train the functional relationship between the system density distribution and various parameters instead of solving partial differential equations to obtain the operator. By replacing the complex functional process with the DeepONet framework, our model can directly compute the ion distribution at the electrode/electrolyte interface and subsequently predict other properties of the system, such as adsorption capacity, differential capacitance, electrolyte phase diagram and interface screening effect (Figure 1D). The results demonstrate that the density distribution predicted by the DeepMT model is consistent with the CDFT results, and computational efficiency is significantly improved.

2. Results and discussion

The system we simulated is a classical electrode/electrolyte system, where the electrolyte with a concentration of c is in contact with a flat electrode with a potential of φ. The electrolyte is described by the restricted primitive model (RPM). For our research system, we considered the case of homogeneous ion concentration of 0–3 mol/L, electrode potential range of $-1\ V$ to $+1$ V, anion and cation diameters of 0.5–1.0 nm in the training data, which covers the electrode/electrolyte properties in most cases from dilute to concentrated solutions. Different dielectric constants were set to simulate different electrolyte environments from aqueous solution to ion liquids. When calculating the density through the mesoscopic thermodynamic model, we sampled the density value at every 0.01 nm position and obtained about 5754710 sets of data for training (Figure S4). The temperature is consistent at 273 K under all conditions. Both anions and cations carry a unit charge, regardless of the van der Waals force between ions. To train the DeepONet framework, we use the Adamax optimizer with a learning rate of 0.0001 and train 1000 iterations. The batch size is set to 256, with ReLU utilized as the activation function and Huber loss employed as the loss function. More parameter descriptions and parameter settings can be found in Supporting Information. The losses of the training data and the test data during training process are shown in Figure 2A, where the orange line represents the training error, and the green line represents the test error. Based on the training outcomes, both the error of training data and the error of test data demonstrate substantial convergence. This indicates that our network architecture exhibits robust convergence properties and effective extrapolation capabilities. The parity plot comparing the predicted results of the DeepMT model with the calculated density distribution from the CDFT are shown in Figure 2B. This graph is drawn using the values of the density distribution in the test set. The results indicate that the predicted data are predominantly clustered around the diagonal line, demonstrating that the neural network exhibits high accuracy.

During the CDFT calculations, we employed the Picard iteration[29] method for iterative computations. To begin the Picard iteration, an initial density distribution ρ_0 is provided. This initial distribution is used to compute different excess

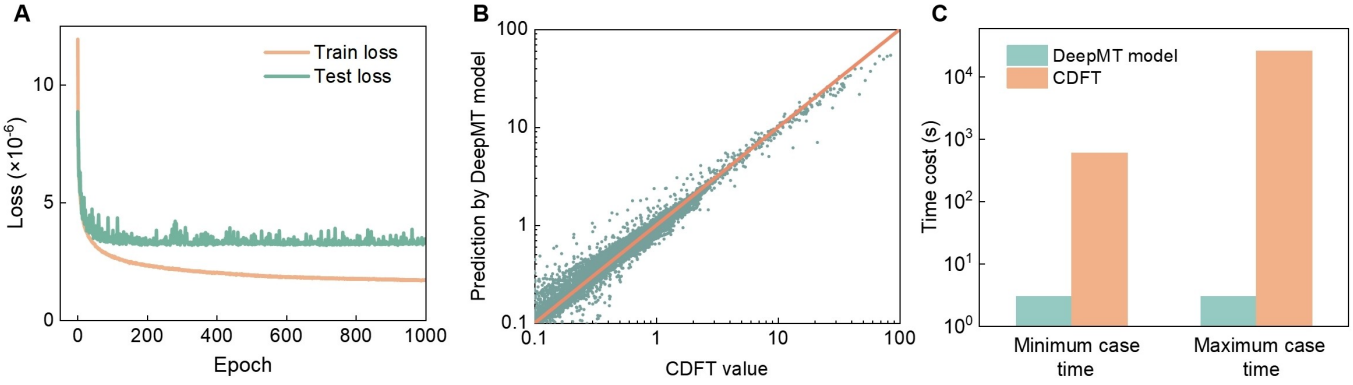

Figure 2. Training status of the DeepMT model. (A) The train error and test error of the neural network, which were described by using smoothed mean absolute error Huber loss. (B) Parity plot of the DeepMT predicted value against the CDFT calculation value. (C) Comparison of the time consumption of DeepMT prediction and direct theoretical calculations of CDFT under different parameter combinations.

free energies of the solution system. Subsequently, excess free energy is utilized to obtain an updated density distribution ρ_i. The difference between ρ_0 and ρ_i is then evaluated to determine if it satisfies the convergence criteria. If the criteria are met, the density value is output as the ion distribution of the system. If not, the input density distribution is updated using an iteration parameter, and the process is repeated until the convergence requirement is fulfilled. To compare the time required for the DeepMT model in predicting the ion distribution with the time taken by the CDFT, we counted the computation time under multiple parameter combinations and compared the time taken by the most time-consuming and least time-consuming cases among all the calculation cases, as shown in Figure 2C. According to our statistical results, the computation time of the CDFT is very sensitive to the parameters used in the above calculations, and the computation time ranges from approximately 600 seconds to 260,000 seconds. The prediction of the interface ion distribution can be completed in just 3 seconds using the DeepMT framework. Therefore, the rate predicted by the DeepMT model is 2–4 orders of magnitude higher than that obtained through direct theoretical calculations. The rapid and accurate computation of the mesoscopic thermodynamic model using neural networks is of great significance for the study of interfacial double layers. By significantly reducing computation time while maintaining high accuracy, neural networks enable efficient analysis and can be seamlessly integrated with other processes such as thermal transfer, flow dynamics, and surface reactions.

The density distribution results predicted by the DeepMT model were initially compared with those calculated using the CDFT, as shown in Figure 3. We evaluate the accuracy of ion density distribution predictions over different bulk concentrations, electrode potentials, and ion diameters. For the sake of convenience, here we use the cation density value as an indicator to evaluate the predictive ability of the DeepMT model. In comparison with direct theoretical calculations of CDFT, the DeepMT model's predictions align closely with the theoretical values of the CDFT. At the electrode/electrolyte interface, in the absence of additional chemical effects, the thermodynamic properties of the electrolyte system are primarily governed by electrostatic effects and volume exclusion. The electrostatic repulsion and attraction between the ions near the electrode surface causes ions to either aggregate or repel each other, while volume exclusion prevents ions from approaching each other too closely in space, resulting in localized high and low concentration regions. This local inhomogeneity can lead to an oscillatory distribution of ion density.[29] As shown in Figure 3A, increasing bulk concentrations enhances the effect of the electrostatic repulsion and attraction between ions, leading to oscillatory distributions at high concentrations and monotonic decreases at low concentrations. Similarly, Figure 3B indicates that at higher electrode potentials, the density distribution also transitions from monotonic to oscillatory, driven by strengthened electrostatic interactions and ion aggregation near the electrode surface, while Figure 3C highlights that larger ion diameters exacerbate repulsive interactions, promoting periodic aggregation. Some theories that describe interface phenomena such as the Poisson–Boltzmann (PB) theory, fail to effectively consider the influence of these complex factors due to their reliance on the continuous medium assumption and homogeneous electrolyte model. Consequently, the obtained ion density distribution at the electrode-electrolyte interface frequently exists a monotonic trend. In contrast, the mesoscopic thermodynamic model can systematically incorporate long-range and short-range ion interactions, as well as volume exclusion effects, enabling it to describe the oscillatory distribution of ions at the interface and potential charge reversal phenomena. These findings are corroborated by MC simulations and MD simulations.[22] Therefore, the DeepMT model can accurately replicate the intricate oscillatory characteristics of density values, demonstrating its exceptional accuracy in predicting interface ion density distribution.

The interfacial distribution of ion density is one of the most basic properties of the electrode-electrolyte interface. Once the ion distribution is obtained, some important physical and chemical properties of the interface can be further obtained. Adsorption is a crucial property for the

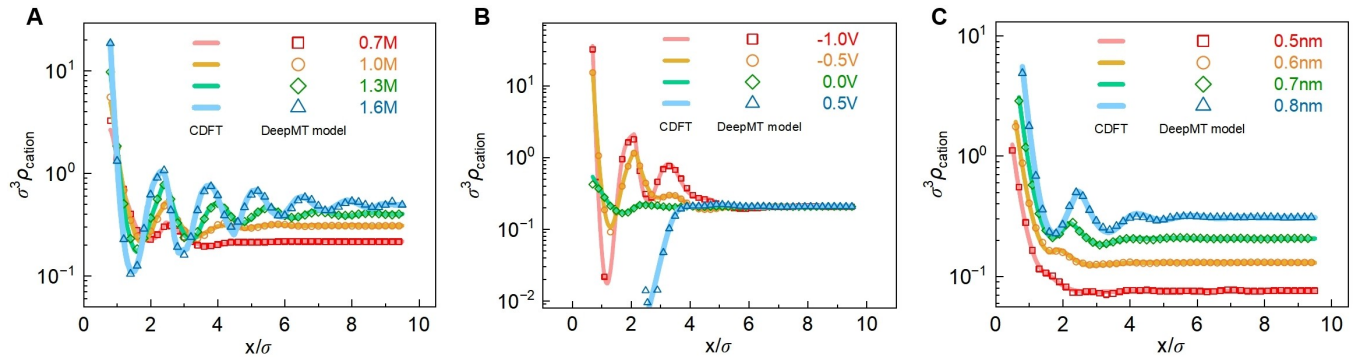

Figure 3. Comparison of cation density distribution predicted by the DeepMT model and calculated by the CDFT at different (A) bulk concentrations (σ=0.7 nm, φ=-0.125 V), (B) electrode potentials (σ=0.8 nm, c=1 M), and (C) ion diameters (φ=-0.125 V, c=1 M). The lines represent calculation results of the CDFT, and the dots represent prediction results of the DeepMT model. The $\sigma^3\rho$ is the reduced ion density.

design and optimization of electrochemical systems because it determines the charge transfer and electric field distribution at the interface. Consistent with the presentation of density distribution results, we now present the neural network's predictions of interface ion adsorption from three perspectives: bulk concentration, electrode potential, and ion diameters. It is found that ion density distribution gradually stabilizes at 5 nm away from the electrode and approaches the homogeneous ion concentration. Consequently, we analyzed ion adsorption specifically within the 0–5 nm range from the electrode/electrolyte interface, focusing exclusively on cation adsorption. As illustrated in Figure 4 A–C, the results on the adsorption behaviors from the DeepMT model and the direct theoretical calculations exist a high degree of consistency under all conditions. This demonstrates the high accuracy of the DeepMT model in describing ion adsorption. Specifically, as bulk concentration increases, the adsorption capacity exhibits a gradual upward trend, with being nearly proportional to the bulk concentration (Figure 4A). As the electrode potential increases from −1 V to 0 V, the adsorption capacity of cations exists a steep decreasing trend. When the potential becomes positive and 0 V to +1 V, the adsorption curve displays a smooth decreasing trend (Figure 4B). The difference is mainly because when the electrode is negatively charged, a significant number of cations are attracted to the electrode surface, resulting in a high concentration of cations. As the potential increases towards zero, the electrode's ability to attract cations is weakened, leading to a rapid decrease in cation concentration. Conversely, when the electrode is positively charged, cations are repelled, but the lower concentration of cations and the attraction of accumulated anions make the adsorption capacity of cations decrease more slowly. The adsorption results in Figure 4C reveal that as the ion diameter increases, it appears a gradual decrease in the adsorption capacity. Concurrently, the slope of the adsorption curve diminishes with increasing ion diameter. This is because larger ion volumes lead to a greater repulsive interaction between ions, resulting in a reduction of ion density at the interface. Consequently, the adsorption capacity of ions change inversely with ion diameter. The downward trend of the curves also show a high degree of consistency between the DeepMT prediction and the CDFT calculation.

The charge-voltage curve can show the charge–discharge behavior of electrode-electrolyte interfaces at different voltages. These curves are used to evaluate the capacity, energy density and energy efficiency of electrochemical devices (such as supercapacitors and batteries). Therefore, we also show the results of the DeepMT model and the direct theoretical calculations of CDFT for charge-voltage curves, as shown in Figure 4D-F. Here, the charge-potential curves over three diameters are presented. The neural network predictions closely overlap with the theoretical calculations. For each diameter, the surface charge increases with absolute electrode potential and gradually approaches saturation. It can be also observed that smaller ion diameters leads to a large slope of the charge-potential curve, corresponding to a strong response of surface charge to the increase of electrode potential. This is because the ions with smaller diameters have a weaker steric effect, which accelerates the change of surface charge to the electrode potential.

According to the charge-potential diagram, we can obtain the differential capacitance of the system by calculating the slope of the curves. As shown in Figure 4G-I, it illustrates how the differential capacitance varies with the electrode potential for three distinct ion diameters. These plots provide critical insights into electrochemical behavior at the electrode-electrolyte interface. At small ion diameters (Figure 4G), the differential capacitance shows a clear peak at zero potential. As absolute potential increases, the differential capacitance gradually decreases, which is symmetrically distributed on both sides of the zero potential point. This is mainly because differential capacitance reflects the sensitivity of charge at electrode/electrolyte interface to the change in potential. When the electrode potential is 0, the distribution of anions and cations is relatively uniform. While as the electrode potential gradually increases, the electrode surface attracts more oppositely charged ions. The ionic layer becomes more compact, so the differential capacitance gradually decreases. As the ion diameter increases progressively (Figure 4H, I), the peak of the differential capacitance at zero potential decreases, and the

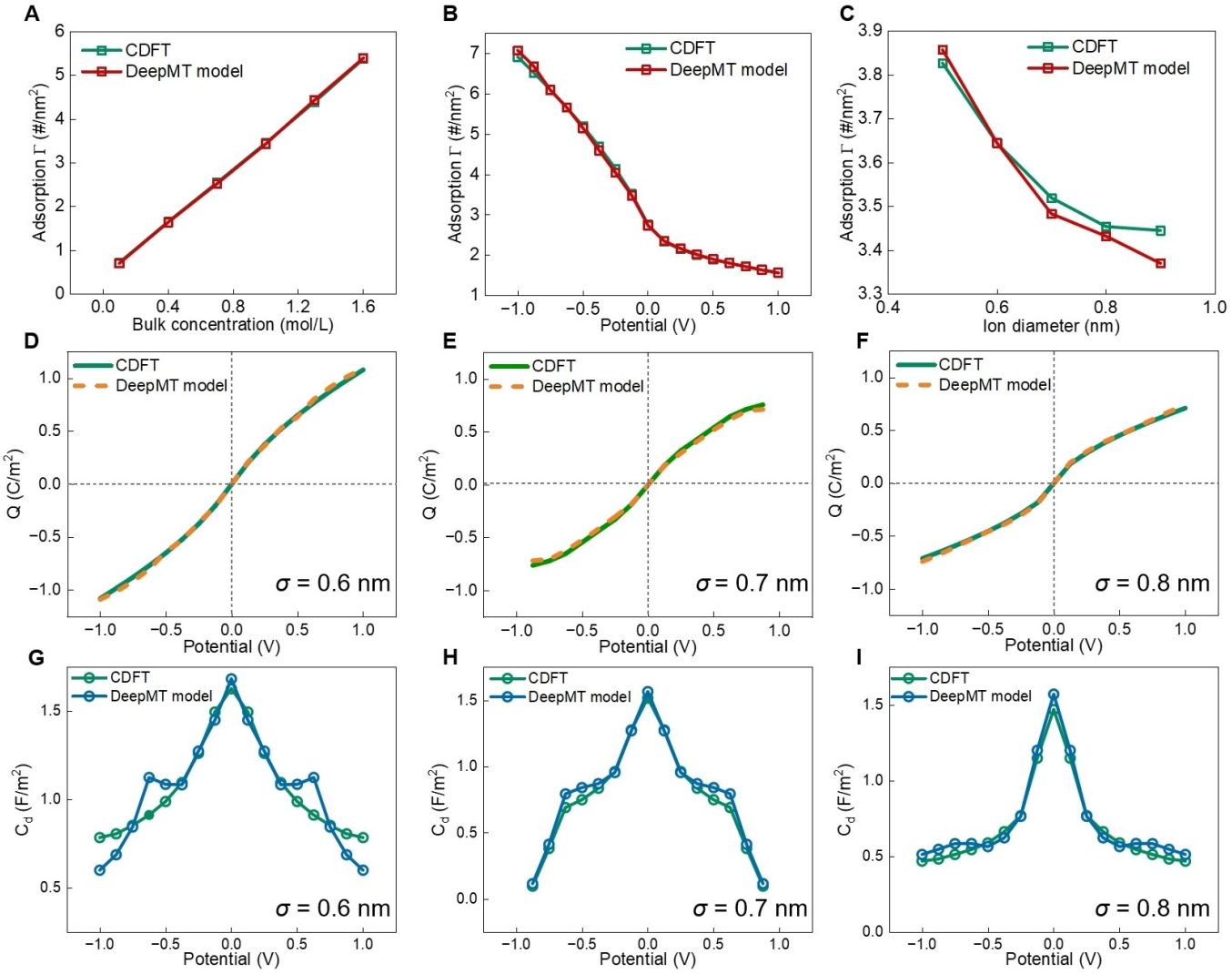

Figure 4. Comparison of interfacial properties predicted by the DeepMT model and calculated using the CDFT. (A) Adsorption capacity as a function of bulk concentration when the electrode potential is −0.125 V and ion diameters are 0.7 nm. (B) Effect of electrode potential on adsorption capacity when bulk concentration is 1 mol/L and ion diameters are 0.8 nm. (C) Adsorption capacity at different ion diameters when bulk concentration is 1 mol/L and electrode potential is −0.125 V. (D–F) Charge-voltage curves with ion diameters of 0.6, 0.7, and 0.8 nm when bulk concentration is 1 mol/L. (G–I) Differential capacitance curves with ion diameters of 0.6, 0.7, and 0.8 nm when bulk concentration is 1 mol/L.

peak width decreases. This is because the ions with larger diameters have a greater repulsion interaction and a lower charge density, so they have a lower capacity for charge exchange, resulting in smaller differential capacitance values at same potential. Except for a few points, the trend of the model prediction value and the theoretical value is relatively similar. Since the differential capacitance value is derived from the charge-potential curve, the charge value predicted by the DeepMT model may be large or small, and the slope of a few points of the charge-potential curve may differ from the theoretical calculation. But in general, the DeepMT model also have strong predictive power for differential capacitance.

Finally, we make some prospects for the application of the DeepMT model. In addition to the relatively simple interface properties as mentioned above, the DeepMT model can also be used to study more complex interface properties (Figure 1D). For example, the phase diagram can be drawn by determining the ion density distribution at various temperatures, then using it to calculate the chemical potential and grand potential at different concentrations for the identification of the phase equilibrium point.[30] This unconventional phase diagram reveals the phase change behavior of ions in a slit pore under different temperature and concentration conditions.[31] The gas-like phase and liquid-like phase in the phase diagram correspond to the stable phases of the system under low-density and high-density states, respectively.[32] Phase diagram research is crucial to understanding the phase behavior of complex electrolytes in confined spaces and under electric fields. Predicting and analyzing phase diagrams through the DeepMT model not only help to overcome the limitations of experimental measurements, but also provide important

theoretical support for the design and optimization of electrochemical applications.

Moreover, the DeepMT model can also be applied to investigate the screening behaviors of confined electrolytes (Figure 1D). The screening length is derived by calculating the grand potential from the density distribution and obtaining the system's interface pressure.[33] The screening length in an electrolyte describes the extent to which the electrostatic field generated by electrode charges is attenuated by the surrounding oppositely charged ions.[34] It defines the spatial range over which the electrode exerts a significant electrostatic influence in the electrolyte, beyond which the effect of the electric field is rapidly diminished. Electrolyte screening is affected by many factors, such as electrostatic effect, steric effect, solvent effect, and association effect. In our early work,[35] we used CDFT to investigate the effect of ion association on the screening effect, but the involved electrolyte environment was still relatively simple. The DeepMT model offers the potential to account for more complex solution environments and interionic interactions, enabling a more comprehensive study of electrolyte screening effects.

3. Conclusion

In this work, we combine a deep neural network with the mesoscopic thermodynamic model to realize the fast calculation of EDL structure and properties. The proposed DeepMT model can accurately calculate the interfacial ion density under different conditions, capture the ion oscillation distribution and charge flipping phenomenon. The computational efficiency of the DeepMT model is improved by 2–4 orders of magnitude compared with the direct theoretical calculation. The adsorption capacity, surface charge and differential capacitance predicted by the DeepMT model are also very close to the calculated values of the CDFT, which indicates that the DeepMT model also has a strong ability to predict the properties of electrode/electrolyte interface. Our work highlights the importance of bridging microscopic complex interactions and macroscopic external field effects in describing ion distribution and predicting interface properties. The model provides a novel approach to the AI-for-interface issue, contributing to the development of the communities of CDFT, mesoscopic thermodynamics and electrochemical interfaces. However, the current model is still based on a one-dimensional system with limited factors considered, making it challenging to fully describe interfacial properties under more complex conditions. Combining the deep neural network with more methods such as molecular dynamics (MD) simulations to achieve rapid prediction of interfacial properties under broader conditions represents a promising direction for future research.

Acknowledgements

This work is sponsored by the National Key R&D Program of China (2022YFB4602101), the Fundamental Research Funds for the Central Universities (2022ZFJH004, and 2024SMECP05), the National Natural Science Foundation of China (22278127, and 22378112), the Shanghai Pilot Program for Basic Research (22T01400100-18), the China Postdoctoral Science Foundation (2024 M750909), and the Postdoctoral Fellowship Program of CPSF (GZC20230801). H. T. and S. W. thank Pan Huang for the help in the implementation of the DeepONet method.

Conflict of Interest

The authors declare no conflict of interest.

Data Availability Statement

The data that support the findings of this study are available from the corresponding author upon reasonable request.

Keywords: electrode-electrolyte interface · structure and properties · classical density functional theory · mesoscopic thermodynamic model · deep neural network

[1] a) A. E. Nel, L. Mädler, D. Velegol, T. Xia, E. M. V. Hoek, P. Somasundaran, F. Klaessig, V. Castranova, M. Thompson, *Nat. Mater.* **2009**, *8*, 543–557; b) D. I. O. Egbe, A. Jahanbani Ghahfarokhi, M. Nait Amar, O. Torsæter, *Nat. Resour.* **2021**, *30*, 519–542.
[2] a) Q. Zhang, Z. Song, X. Sun, Y. Liu, J. Wan, S. B. Betzler, Q. Zheng, J. Shangguan, K. C. Bustillo, P. Ercius, P. Narang, Y. Huang, H. Zheng, *Nature.* **2024**, *630*, 643–647; b) J. T. Mefford, A. R. Akbashev, M. Kang, C. L. Bentley, W. E. Gent, H. D. Deng, D. H. Alsem, Y.-S. Yu, N. J. Salmon, D. A. Shapiro, P. R. Unwin, W. C. Chueh, *Nature.* **2021**, *593*, 67–73.
[3] a) X. Liu, A. Mariani, H. Adenusi, S. Passerini, *Angew. Chem. Int. Ed.* **2023**, *62*, e202219318; b) S. Krem, M. Lee, S. Sam, W. Sung, D. Kim, *J. Phys. Chem. Lett.* **2021**, *12*, 3417–3423; c) C. F. Chamberlayne, R. N. Zare, J. G. Santiago, *J. Phys. Chem. Lett.* **2020**, *11*, 8302–8306; d) J. Huang, Y. Zhang, M. Li, A. Groß, S. Sakong, *J. Phys. Chem. Lett.* **2023**, *14*, 2354–2363.
[4] O. M. Magnussen, A. Groß, *J. Am. Chem. Soc.* **2019**, *141*, 4777–4790.
[5] a) J. Hou, B. Xu, Q. Lu, *Nat. Commun.* **2024**, *15*, 1926; b) Q. Wu, C. Dai, F. Meng, Y. Jiao, Z. J. Xu, *Nat. Commun.* **2024**, *15*, 1095.
[6] H. Helmholtz, *Annalen der Physik.* **1853**, *165*, 211–233.
[7] M. Gouy, *J. Phys. Theor. Appl.* **1910**, *9*, 457–468.
[8] D. L. Chapman, *Philos. Mag.* **1913**, *25*, 475–481.
[9] O. Stern, *Angew. Phys. Chem.* **1924**, *30*, 508–516.
[10] D. C. Grahame, *Chem. Rev.* **1947**, *41*, 441–501.
[11] a) M. Becker, P. Loche, M. Rezaei, A. Wolde-Kidan, Y. Uematsu, R. R. Netz, D. J. Bonthuis, *Chem. Rev.* **2024**, *124*, 1–26; b) H. Du, K. Song, M. Yang, P. Huang, W. Chen, *ChemSusChem.* **2023**, *16*, e202300708; c) T. Luo, K. Liu, J. Fu, S. Chen, H. Li, H. Pan, M. Liu, *Adv. Energ. Sust. Res.* **2023**, *4*, 2200148.

[12] C. Liu, Y. Bai, W. Li, F. Yang, G. Zhang, H. Pang, *Angew. Chem. Int. Ed.* **2022**, *61*, e202116282.
[13] M.-J. Zhu, J.-B. Pan, Z.-Q. Wu, X.-Y. Gao, W. Zhao, X.-H. Xia, J.-J. Xu, H.-Y. Chen, *Angew. Chem. Int. Ed.* **2018**, *57*, 4010–4014.
[14] L. Jia, Z. H. Guo, L. Li, C. Pan, P. Zhang, F. Xu, X. Pu, Z. L. Wang, *ACS Nano.* **2021**, *15*, 19651–19660.
[15] a) Y. Litman, K.-Y. Chiang, T. Seki, Y. Nagata, M. Bonn, *Nat. Chem.* **2024**, *16*, 644–650; b) B. Lyu, D. Li, Q. Wang, J. Sun, Q. Xiong, D. Zhang, H. Su, W. C. H. Choy, *Angew. Chem. Int. Ed.* **2024**, *63*, e202408726; c) Q. Guo, G. Teri, W. Mo, J. Huang, F. Liu, M. Ye, D. Fu, *Energy Environ.* **2024**, *17*, 2888–2896.
[16] a) H. Ni, R. C. Amme, *J. Colloid Interface Sci.* **2003**, *260*, 344–348; b) S. Yabunaka, A. Onuki, *Phys. Rev. Lett.* **2017**, *119*, 118001.
[17] a) Y. S. Park, I. S. Kang, *J. Electroanal. Chem.* **2021**, *880*, 114923; b) J. J. Bikerman, *Philos. Mag.* **1942**, *33*, 384–397; c) D. Henderson, D. Boda, *Phys. Chem. Chem. Phys.* **2009**, *11*, 3822–3830; d) A. A. Kornyshev, *J. Phys. Chem. B.* **2007**, *111*, 5545–5557; e) A. C. Maggs, R. Podgornik, *Soft Matter.* **2016**, *12*, 1219–1229.
[18] L. Scalfi, M. Salanne, B. Rotenberg, *Annu. Rev. Phys. Chem.* **2021**, *72*, 189–212.
[19] D. Bedrov, J.-P. Piquemal, O. Borodin, A. D. MacKerell, Jr., B. Roux, C. Schröder, *Chem. Rev.* **2019**, *119*, 7940–7995.
[20] D. J. Adams, *Mol. Phys.* **1974**, *28*, 1241–1252.
[21] R. Evans, T. J. Sluckin, *Mol. Phys.* **1980**, *40*, 413–435.
[22] a) W. Silvestre-Alcantara, L. B. Bhuiyan, J. Jiang, J. Wu, D. Henderson, *Mol. Phys.* **2014**, *112*, 3144–3151; b) J. W. Lee, R. H. Nilson, J. A. Templeton, S. K. Griffiths, A. Kung, B. M. Wong, *J. Chem. Theory Comput.* **2012**, *8*, 2012–2022.
[23] A. Härtel, *J. Phys.: Condens. Matter.* **2017**, *29*, 423002.
[24] J. Mairhofer, J. Gross, *Fluid Phase Equilib.* **2017**, *444*, 1–12.
[25] a) D. Fan, L. Yang, Z. Wang, M. S. Triantafyllou, G. E. Karniadakis, *Proc. Natl. Acad. Sci.* **2020**, *117*, 26091–26098; b) K. Duraisamy, G. Iaccarino, H. Xiao, *Annu. Rev. Fluid Mech.* **2019**, *51*, 357–377; c) G. M. Martins, F. C. Braga, P. P. de Castro, T. J. Brocksom, K. T. de Oliveira, *Chem. Commun.* **2024**, *60*, 3226–3239; d) P. Hou, Y. Tian, Y. Xie, F. Du, G. Chen, A. Vojvodic, J. Wu, X. Meng, *Angew. Chem. Int. Ed.* **2023**, *62*, e202304205.
[26] K. Hornik, M. Stinchcombe, H. White, *Neural Netw.* **1989**, *2*, 359–366.
[27] a) L. Shang Chun, M. Oettel, *SCIPOST PHYS.* **2019**, *6*; b) P. Cats, S. Kuipers, S. de Wind, R. van Damme, G. M. Coli, M. Dijkstra, R. van Roij, *APL. Materials.* **2021**, *9*, 031109; c) F. Sammüller, S. Hermann, D. de Las Heras, M. Schmidt, *Proc. Natl. Acad. Sci.* **2023**, *120*, e2312484120; d) A. Simon, J. Weimar, G. Martius, M. Oettel, *J. Chem. Theory Comput.* **2024**, *20*, 1062–1077; e) J. Dijkman, M. Dijkstra, R. Roij, M. Welling, J.-W. v. d. Meent, B. Ensing, **2024**.
[28] L. Lu, P. Jin, G. Pang, Z. Zhang, G. E. Karniadakis, *Nat. Mach. Intell.* **2021**, *3*, 218–229.
[29] D.-e. Jiang, D. Meng, J. Wu, *Chem. Phys. Lett.* **2011**, *504*, 153–158.
[30] S. Kondrat, M. Bier, L. Harnau, *J. Chem. Phys.* **2010**, *132*, 184901.
[31] a) K. Liu, P. Zhang, J. Wu, *J. Chem. Phys.* **2018**, *149*, 234708; b) K. Liu, J. Wu, *J. Chem. Phys.* **2020**, *152*, 054708.
[32] J. Cheng, J. Xu, S. Wang, X. Chen, C. Lian, H. Liu, *AIChE Journal.* **2024**, *70*, e18496.
[33] P. Cats, R. Evans, A. Härtel, R. van Roij, *The Journal of Chemical Physics.* **2021**, *154*, 124504.
[34] a) M. A. Gebbie, M. Valtiner, X. Banquy, E. T. Fox, W. A. Henderson, J. N. Israelachvili, *Proc. Natl. Acad. Sci.* **2013**, *110*, 9674–9679; b) M. A. Gebbie, H. A. Dobbs, M. Valtiner, J. N. Israelachvili, *Proc. Natl. Acad. Sci.* **2015**, *112*, 7432–7437; c) J. Yang, S. Kondrat, C. Lian, H. Liu, A. Schlaich, C. Holm, *Phys. Rev. Lett.* **2023**, *131*, 118201; d) A. Härtel, M. Bültmann, F. Coupette, *Phys. Rev. Lett.* **2023**, *130*, 108202.
[35] S. Wang, H. Tao, J. Yang, J. Cheng, H. Liu, C. Lian, *J. Phys. Chem. Lett.* **2024**, *15*, 7147–7153.

Manuscript received: September 25, 2024
Accepted manuscript online: October 18, 2024
Version of record online: November 13, 2024